nature physics

ARTICLES

PUBLISHED ONLINE: 3 APRIL 2017 | DOI: 10.1038/NPHYS4084

Inducing superconducting correlation in quantum Hall edge states

Gil-Ho Lee[1], Ko-Fan Huang[1], Dmitri K. Efetov[2,3], Di S. Wei[1], Sean Hart[1†], Takashi Taniguchi[4], Kenji Watanabe[4], Amir Yacoby[1] and Philip Kim[1*]

The quantum Hall (QH) effect supports a set of chiral edge states at the boundary of a two-dimensional system. A superconductor (SC) contacting these states can provide correlations of the quasiparticles in the dissipationless edge states. Here we fabricated highly transparent and nanometre-scale SC junctions to graphene. We demonstrate that the QH edge states can couple via superconducting correlations through the SC electrode narrower than the superconducting coherence length. We observe that the chemical potential of the edge state exhibits a sign reversal across the SC electrode. This provides direct evidence of conversion of the incoming electron to the outgoing hole along the chiral edge state, termed crossed Andreev conversion (CAC). We show that CAC can successfully describe the temperature, bias and SC electrode width dependences. This hybrid SC/QH system could provide a novel route to create isolated non-Abelian anyonic zero modes, in resonance with the chiral edge states.

Inducing superconducting correlations via the proximity effect into a two-dimensional electron gas (2DEG) in the quantum Hall (QH) regime has been a long-standing challenge and has attracted renewed attention due to its promise for realizing non-Abelian zero modes[1–5]. Unlike conventional conductors, the 2DEG can exhibit an insulating incompressible bulk electronic state under perpendicular quantizing magnetic fields. In this QH regime, the conduction of electric charge occurs only along the edges via one-dimensional (1D) chiral edge states, which the SC can make contacts to. To realize the hybrid system of QH and SC, the upper critical field of the SC needs to be high enough such that Cooper pairs in the SC are correlated mostly to the quasiparticles in well-developed 1D QH edge states. The experimental realization of such hybrid systems often encounters challenges in semiconductor 2DEGs due to the formation of large Schottky barriers at the SC/semiconductor interfaces[6]. Graphene is a compelling candidate for the SC/QH platform, since the zero bandgap of graphene ensures Ohmic contacts for most metals, including SCs with high upper critical fields. Highly transparent SC/graphene interfaces have been demonstrated with strong superconducting proximity interactions and Josephson couplings[3,7–13]. In addition, high-mobility hBN-encapsulated graphene channels exhibit integer and fractional QH effects[14,15] at much lower magnetic field than the upper critical field of a few select SCs.

Negative non-local voltages from the Andreev process

The microscopic picture of charge flow across the SC/QH system can be described by extending the Andreev process[16–18] between a SC and a normal conductor. Figure 1a depicts local Andreev reflection at zero magnetic field. An electron with energy (eV), which is smaller than the superconducting gap (Δ), can enter the ground drain SC electrode to form a Cooper pair, while retro-reflecting a hole back to the source of the electron. In the presence of a magnetic field, however, the chiral nature of the QH edge state forces the converted hole to keep flowing with the same chirality as the incoming electron. Note that the hole has the same chirality as the electron, because the signs of its charge and mass are both opposite to those of the electron. There can be two different regimes in this Andreev process, depending on the width of the SC electrode (W) compared with the superconducting coherence length (ξ_s). When $W \gg \xi_s$, the electron and hole will propagate along the edge of the SC electrode forming an Andreev edge state (AES)[16–18] (Fig. 1b). In a quasi-classical picture, the AES is an alternating skipping orbit of electrons and holes. Unless the probability of each Andreev reflection (P_{AR}) is very close to zero or unity, the AES quickly becomes an equal mixture of electrons and holes after a few bounces (Supplementary Fig. 1). The resulting mixed AES along the ground SC (that is, at zero chemical potential) carries the averaged chemical potential equal to zero. However, when $W \ll \xi_s$ the converted hole can tunnel through the SC electrode and continue to flow on the other side of the QH edge state, a process termed as crossed Andreev conversion (CAC)[19,20] (Fig. 1c). Note that in the CAC process, the converted hole in the downstream carries negative (electron) chemical potential. Therefore, unlike the case of the AES, the spatial separation of electrons and holes in CAC facilitates their independent detection by measuring the chemical potential of upstream and downstream QH edge states with respect to the ground SC electrode, which we demonstrate in this paper. Interestingly, in the asymptotic limit of $W \ll \xi_s$ and a long finger-like SC electrode whose length $L \gg hv_F/\Delta$, the CAC picture corresponds to creating two non-Abelian anyons in resonance with the QH edge state[4,5,19,21–25]. Here, h is Planck's constant and v_F is the Fermi velocity of QH edge states. The counter-propagating QH edge modes along both sides of the finger electrode are coupled by the SC, creating two zero modes: one in resonance with the QH edge and the other at the end of the SC finger (inset of Fig. 1c).

[1]Department of Physics, Harvard University, Cambridge, Massachusetts 02138, USA. [2]Department of Electrical Engineering, M.I.T., Cambridge, Massachusetts 02138, USA. [3]ICFO-Institut de Ciencies Fotoniques, The Barcelona Institute of Science and Technology, 08860 Castelldefels (Barcelona), Spain. [4]National Institute for Materials Science, Namiki 1-1, Tsukuba, Ibaraki 305-0044, Japan. [†]Present address: Department of Physics, Stanford University, Stanford, California 94305, USA. *e-mail: pkim@physics.harvard.edu

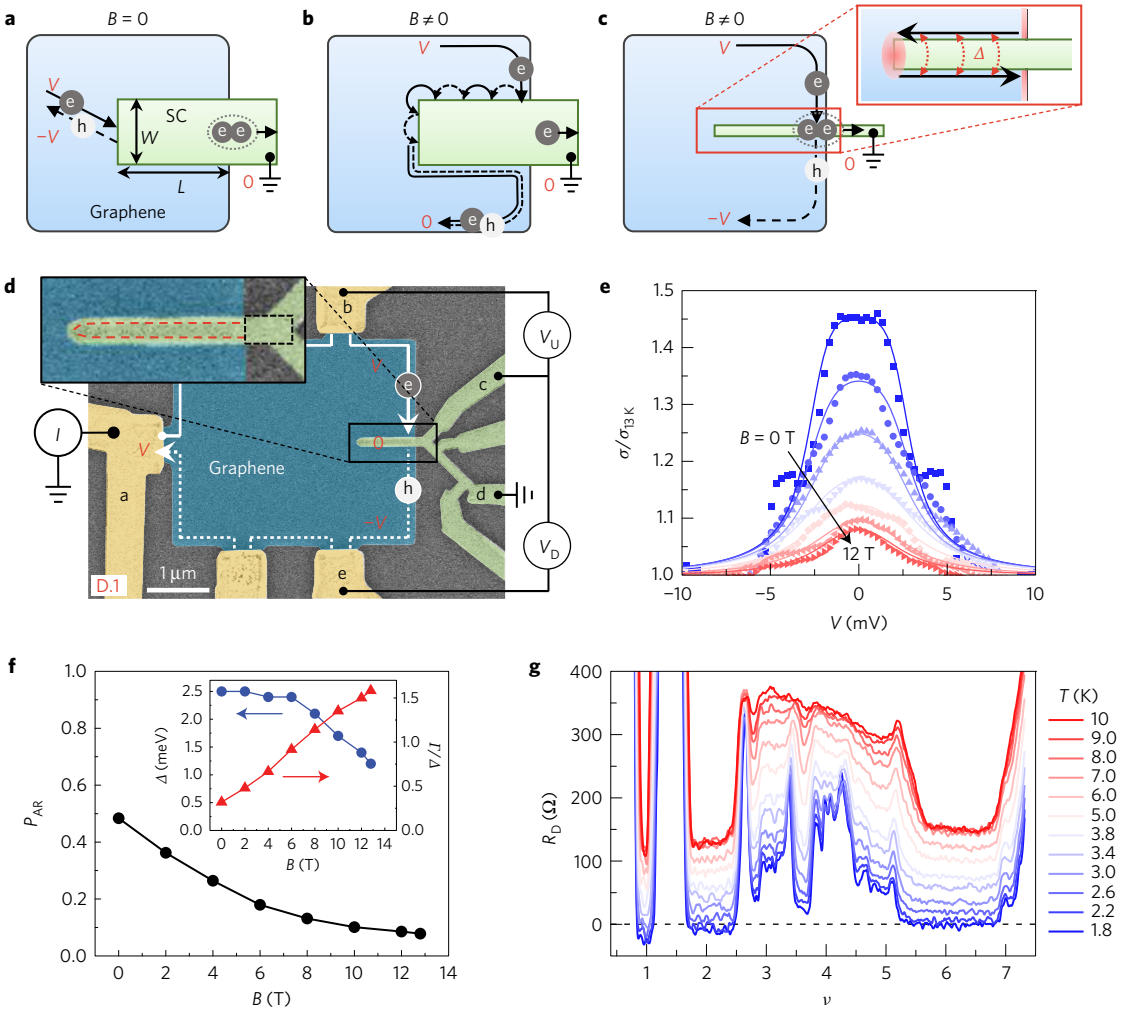

Figure 1 | Magnetic field dependence of Andreev reflection. a–c, Schematic diagram of Andreev pairs of electrons and holes without an external magnetic field (**a**), and in the QH regime with a wide superconductor (**b**) or a narrow superconductor (**c**). Inset of **c**, counter-propagating QH edge states are coupled via the superconducting gap (Δ), resulting in non-Abelian anyonic zero modes at the ends of the NbN electrode (red ellipse). *V*, voltage; e, electron; h, hole. **d**, False-colour scanning electron microscopy (SEM) image of the device D.1 with measurement configurations. Ti/Au normal electrodes (yellow) and a NbN superconducting electrode (green) contact the graphene Hall bar (blue). Inset, 1D NbN contact to the graphene edge is highlighted with a dashed red line. Note that the graphene/NbN contact is positioned slightly more inwards than the boundary shown in the SEM image (see schematic of the cross-section in the lower inset of Fig. 4). The distance between two graphene/NbN contacts is estimated to be 50 nm. A black dashed rectangle highlights the NbN segment contributing to the downstream resistance. V_U, upstream chemical potential; V_D, downstream chemical potential; *I*, current. **e**, The differential conductance of the graphene/NbN interface at $V_{bg} = 60$ V, under various magnetic fields. The data taken at $T = 1.8$ K (σ) are normalized by the data taken at $T = 13$ K ($\sigma_{13\,K}$) when the NbN loses superconductivity. The resistance contribution from the NbN segment represented by the black dashed box in the inset of **d** was subtracted for calculating $\sigma_{13\,K}$. Experimental data (symbols) are fitted to the modified Blonder–Tinkham–Klapwijk theory (solid lines) with a fixed barrier parameter $Z = 0.18$. **f**, The Andreev reflection probability (P_{AR}) at zero bias was calculated from the fitting parameters (inset) obtained by fittings in **e**. **g**, The filling fraction (ν) dependence of the downstream resistance (R_D) at different temperatures with $B = 14$ T.

To measure the chemical potential of QH edge states across the SC electrode, we fabricate a multi-terminal graphene device with a SC drain electrode as shown in Fig. 1d. To obtain a high-quality graphene channel, we encapsulated mechanically exfoliated graphene samples with two hBN crystals using a dry-transfer technique[26]. NbN was chosen for the SC drain contact, since its high upper critical field ($B_{c2} \sim 25$ T) and high critical temperature ($T_c = 12$ K) enable us to experimentally access a wide range of magnetic fields where superconductivity and the QH effect in graphene coexist.

The contact transparency of the SC/graphene interface can be characterized by measuring the differential conductance enhancement, which directly represents local Andreev process (LAP) efficiency. Figure 1e shows the differential conductance ($\sigma = dI_{ad}/dV_{ec}$) of the graphene/NbN interface normalized by the value obtained at the temperature above T_c. Here I_{ad} is the current biased from a to d, and V_{ec} is the voltage drop between electrodes e and c (marked in Fig. 1d). We apply a large backgate voltage of $V_{bg} = 60$ V to put the graphene channel in high filling fractions, away from the well-developed QH regime even at the highest field of $B = 14$ T. The resistance contribution from the graphene channel is negligibly small at this large V_{bg} (see Supplementary Fig. 2a). In this weak field limit, the magnetic-field-dependent σ is determined only by the LAP, not by the modulating density of state (DOS) of the graphene (see Supplementary Fig. 3 for the case when σ is mostly determined by the DOS of graphene in the strong field limit). Thus, σ serves as a useful probe for characterizing the magnetic field dependence on LAP. At zero magnetic field, we observe that the normalized σ exhibits a pronounced zero-bias enhancement up to 45%, which shows that the SC/graphene junction is reasonably transparent. As

B increases, the height of the zero-bias conductance peak reduces, reflecting a reduction of the Andreev reflection probability (P_{AR}). This reduction can be understood considering the excitation of low-energy quasiparticles inside of the SC gap by the magnetic vortices induced by the external magnetic field. The presence of these subgap states allows incident electrons to enter the superconductor without the Andreev process. The Blonder–Tinkham–Klapwijk (BTK) theory that includes a magnetic field[27–32] fits the data with fitting parameters of Δ and energy broadening (Γ), as plotted in the inset of Fig. 1f. Here, Γ is considered in the form of the imaginary part of the energy E by replacing E with $E + i\Gamma$ (see Supplementary Information). Encouragingly, P_{AR} estimated from the fitting parameters is larger than 0.1 for all experimental values of $B \leq 13$ T, approximately following the zero-bias enhancement under the magnetic fields.

Employing a highly transparent SC/graphene contact, the CAC process can be now investigated in dissipationless chiral edge modes in the QH regime of graphene. For this experiment, we performed non-local measurements, monitoring the voltage drop between electrodes e and c (downstream chemical potential, V_D) with current I biased between electrodes a and d. There is no apparent current flow between e and c except along a small segment of the NbN electrode (marked with a black box in the inset of Fig. 1d), which does not contribute to the voltage drop when it is superconducting. In this non-local configuration, the measurement of V_D is free from any local signal that comes from the modulation of the DOS of graphene in the QH regime, and is sensitive only to the Andreev converted holes. Figure 1g shows the downstream resistance ($R_D = V_D/I$) as a function of the filling fraction ν tuned by V_{bg}. The most striking feature in this graph is a negative downstream chemical potential at low T for well-developed QH states of $\nu = 1$, 2 and 6. In the Landauer–Büttiker picture this negative chemical potential corresponds to a contact transmission coefficient of the drain electrode greater than unity, which is hard to interpret without considering the CAC due to the SC electrode (see Supplementary Fig. 4 for the comparison with the similar device without a SC electrode). Non-local transport with negative resistance clearly indicates the presence of crossed Andreev converted holes, namely the coupling between two QH edge states via the narrow SC electrode. Negative R_D is consistently reproduced in five other devices (see Supplementary Fig. 5). However, when the current flows through the bulk part of the graphene ($\nu \neq 1$, 2 or 6) R_D recovers its positive value.

Temperature behaviour of negative non-local voltage

To further quantitatively analyse the CAC, we now discuss the temperature-dependent negative downstream chemical potential for the $\nu = 2$ QH state. Its large Landau energy gap (~100 meV at $B = 8$ T) allows us to study the system below and above T_c without degrading the QH edge state. As shown in Fig. 2a, R_D for the $\nu = 2$ QH state starts to decrease as T decreases only for the range below the onset critical temperature ($T_{c,on} = 8.7$ K). Note that in this temperature range where the superconductivity is not yet fully developed, R_D still contains the positive contribution (R_{NbN}) that stems from a finite resistance of the NbN electrode segment. The contribution from R_{NbN} vanishes in the lower temperature range $T < T_c = 5.2$ K. We note that the positive value of $R_D(T = T_c) = 180\ \Omega$ corresponds to the contact resistance of the SC/graphene channel due to the imperfect contact (see Supplementary Fig. 6 for the discussion of temperature insensitivity of additional series resistance). By comparing R_D at $T > T_{c,on}$ and $T = T_c$, we determine $R_{NbN} \sim 250\ \Omega$, nearly insensitive to temperature $T > T_{c,on}$. This estimation is also in good agreement with the value estimated from the NbN resistance measured from a segment fabricated as a part of the SC electrode in Fig. 2d. While the negative value of R_D is clearly visible without any further analysis, our quantitative

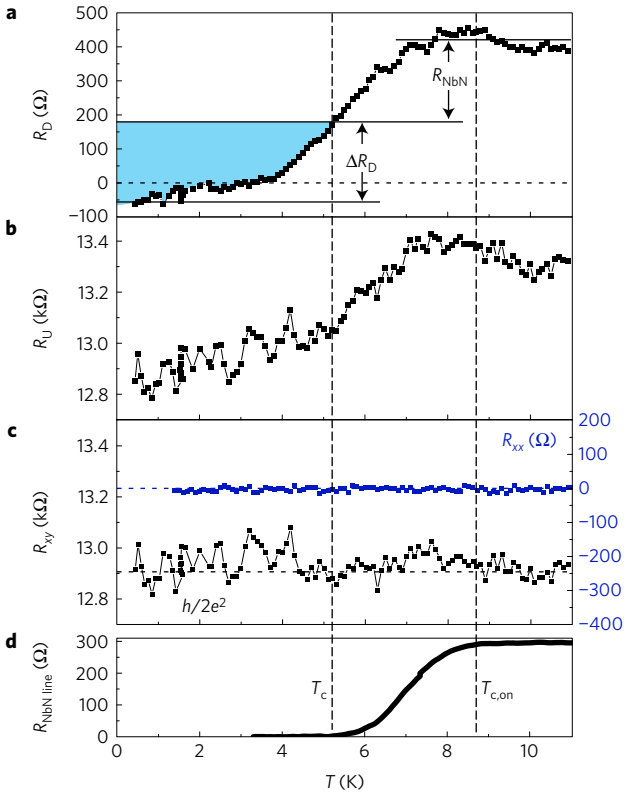

Figure 2 | Temperature dependence of quantum Hall edge chemical potentials at $B = 8$ T. a, The downstream resistance (R_D) at $\nu = 2$ decreases with temperature and eventually becomes negative. **b**, The upstream resistance (R_U) also changes in a similar manner to R_D. **c**, The quantized Hall resistance ($R_{xy} = R_U - R_D = h/2e^2$, black symbols) and vanishing longitudinal resistance (R_{xx}, blue symbols) confirm that the quantum Hall state is stable up to 11 K. **d**, The temperature dependence of the NbN electrode resistance ($R_{NbN\,line}$) exhibits an onset critical temperature $T_{c,on} = 8.7$ K and a critical temperature $T_c = 5.2$ K below which superconductivity in the SC electrode is fully attained. T_c is determined as an intercept between the temperature axis and the tangential line from the point where $R_{NbN\,line}$ reaches 2% of $R_{NbN\,line}(T > T_{c,on})$.

analysis of the finite positive contribution indicates that the full contribution from CAC process is considerably larger than the bare value of R_D. We define the net contribution of CAC process by $\Delta R_D = R_D(T = 0.3\ \text{K}) - R_D(T = T_c)$, which is represented by the shaded area in Fig. 2a. At the lowest temperature of our experiment 0.3 K, $\Delta R_D = -230\ \Omega$, about 4% of the signal expected for a perfectly efficient CAC process ($\Delta R_{D,max} = -h/4e^2$), where e is an electron charge. It is also interesting to note that not only the downstream but also the upstream chemical potential (V_U) changes as the drain electrode becomes superconducting in our constant current-bias scheme. Figure 2b shows the upstream resistance ($R_U = V_U/I$) as a function of temperature. $R_U(T)$ behaves similarly to $R_D(T)$ except for the constant offset independent of the temperature. The difference between R_U and R_D is directly related to the Hall resistance. In our current-biasing scheme, the total conductance ($\sigma = I/V_U$) enhancement by Andreev conversion processes reduces V_U to keep I constant. Therefore, V_U decreases as much as V_D does, and the Hall resistance ($R_{xy} = R_U - R_D$) stays precisely at $h/2e^2$ although R_U and R_D are changed by the CAC (Fig. 2c).

Bias dependence on negative non-local voltage

In principle, the observed negative non-local signal in R_D can possibly be also attributed to other effects, such as ballistic electron transport[26] or viscous electron backflow[33]. To rule out these non-SC

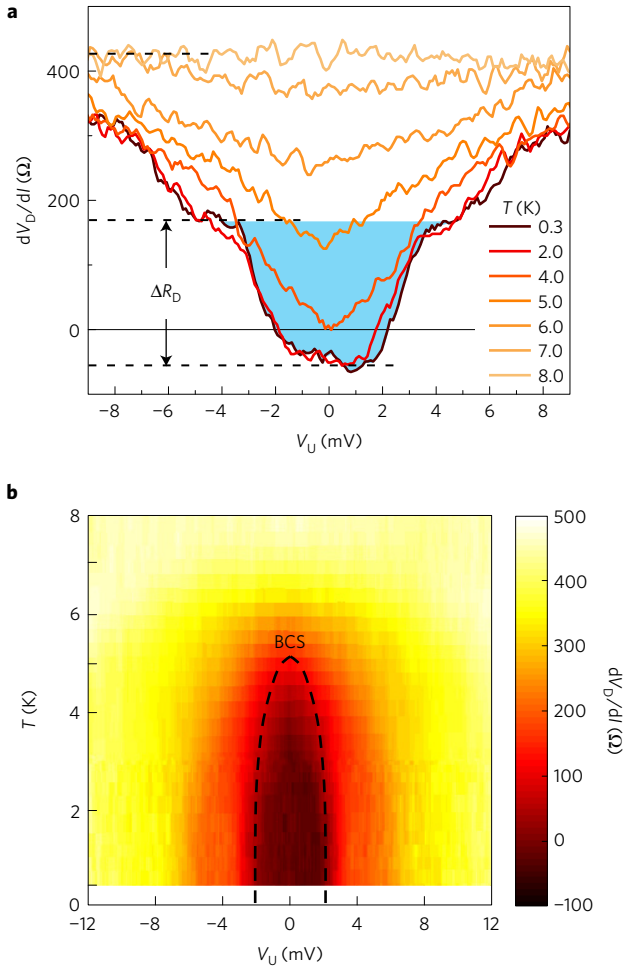

Figure 3 | Bias dependence of the negative response at $B = 8$ T and $\nu = 2$. **a**, The differential downstream resistance (dV_D/dI) as a function of the incident electron voltage (upstream voltage, V_U) at different temperature values, with a.c. excitation current of 1 nA. dV_D/dI becomes positive when $|eV_U| > \Delta$, with the resistance change of $\Delta R_D = -230\ \Omega$ from the zero-bias value. **b**, A colour-coded plot of dV_D/dI shows the temperature dependence of Δ, which follows the temperature dependence of the BCS theory (dashed line).

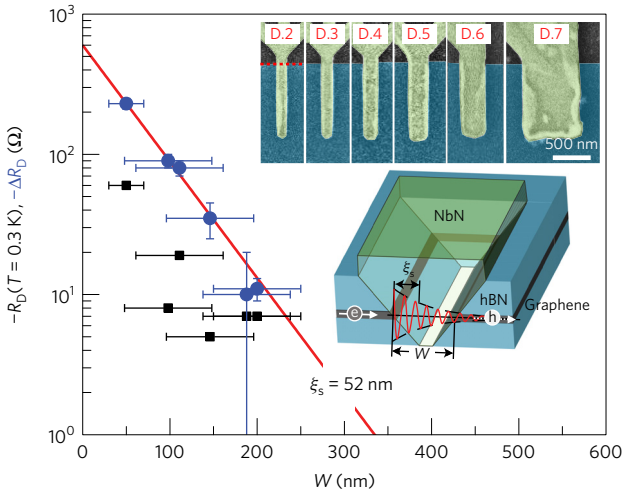

Figure 4 | Exponential width dependence on negative response at $B = 8$ T and $\nu = 2$. The downstream resistance at the base temperature ($R_D(T = 0.3\,K)$, square symbols) and resistance change (ΔR_D, circular symbols) due to the crossed Andreev conversion (CAC) are plotted as a function of the distance between two superconductor (SC)/graphene contacts (W). All devices with $W \lesssim 200$ nm exhibit a finite negative non-local signal. The data points of $R_D(T = 0.3\,K) = 2\ \Omega$ and $\Delta R_D = 0\ \Omega$ for $W = 600$ nm are not visible in the semi-log plot. ΔR_D is fitted to the exponential function of $\Delta R_D = \Delta R_{D,0} \exp[-W/\xi_s]$, with the superconducting coherence length (ξ_s) of NbN and the zero-width-limit value ($\Delta R_{D,0}$) as fitting parameters. Error bars in W are estimated from the roughness of the SC electrodes within the resolution of SEM images. Error bars in ΔR_D represent the uncertainty in determining $R_D(T = T_c)$ that was calculated as $(\partial R_D/\partial T)_{T=T_c} \times \Delta T_c$, where ΔT_c is the difference between T_c and the temperature where $R_{NbN\ line}$ reaches 2% of its normal value. Upper inset, false-coloured SEM images of the devices of $W = 98$, 111, 146, 188, 200, 600 nm, from the left to the right, respectively. Lower inset, a detailed schematic of the cross-section along the dotted red line in the upper inset. Owing to the oblique etching profile of the top hBN, W is smaller than the width of the SC electrode measured by SEM by the thickness of the top hBN.

related scenarios, we further examined the differential resistance (dV_D/dI) as a function of the measured bias voltage V_U (Fig. 3). When the incident electron energy (eV_U) exceeds the SC gap (Δ), electrons can enter the quasiparticle state above the SC gap and the Andreev process probability is rapidly suppressed. As shown in Fig. 3, dV_D/dI sharply turns from a negative value (−50 Ω) to a positive value (180 Ω) as V_U exceeds the crossover voltage about 2 mV. This crossover voltage agrees well with Δ/e, estimated from the independent measurement in the inset of Fig. 1f. We note that the amount by which dV_D/dI sharply increases across the crossover voltage agrees with the value of ΔR_D, independently determined in Fig. 2a. Above this crossover voltage, a broad background develops in dV_D/dI. As we further increase V_U above 5 mV, dV_D/dI approaches the value of R_D at $T > T_{c,on}$ where the superconductivity of the NbN electrode completely vanishes. Indeed, the colour-coded plot of dV_D/dI in Fig. 3b exhibits a Bardeen–Cooper–Schrieffer (BCS)-type temperature dependence on Δ, indicating that R_D is closely related to the superconductivity of the drain electrodes. The large ratio of Δ/k_BT_c (∼4.7) deviating from a BCS value (1.742) could be explained by the breakdown of mean-field approximation due to disorder[34], that is further enhanced by the external magnetic field.

Exponential behaviour with the width of superconductor

The CAC process with different width W allows us to study its tunnelling nature and to estimate the SC coherence length ξ_s. During the Andreev process, a pair of electrons propagates through the superconductor as an evanescent mode, eventually condensing into a Cooper pair within the length scale of ξ_s (lower inset of Fig. 4). For a SC electrode of $W \lesssim \xi_s$, the converted hole has a finite probability of tunnelling through the SC and continuing on to the other side of the QH edge state. Since the evanescent pair wavefunction decays exponentially, the CAC process is suppressed as W increases. To quantify this exponential suppression of the CAC process, we study the ΔR_D found in devices with different W, in the range of 50 to 600 nm. Figure 4 shows $R_D(T = 0.3\,K)$ and ΔR_D obtained from the devices with six different W. Although $R_D(T = 0.3\,K)$ seems to follow an exponential trend, ΔR_D shows better exponential dependence after the correction of trivial contribution from the contact resistance. We fit data to $\Delta R_D(W) = \Delta R_{D,0} \exp(-W/\xi_s)$, where $\Delta R_{D,0}$ and ξ_s are the two fitting parameters corresponding to the maximal CAC efficiency in a zero-width limit and the SC coherence length, respectively. From fitting to the data, we obtain $\xi_s = 52 \pm 2$ nm, which is within the range between expected values in the clean ($\xi_{BCS} = \hbar v_F^S/\pi\Delta \sim 200$ nm) and dirty limits $[(\xi_{BCS} l_{mfp})^{1/2} \sim 10$ nm], with the Fermi velocity of NbN $v_F^S = 1.8 \times 10^6\ ms^{-1}$, $\Delta = 1.8$ meV at $B = 8$ T measured in Fig. 1e, and mean free path of $l_{mfp} = 0.3$ nm (refs 35,36). We note that $\Delta R_{D,0} = -600 \pm 27\ \Omega$ is still well below the ideal value of $\Delta R_{D,max} = -h/4e^2$, presumably due to the presence

of the magnetic-field-induced quasiparticle excitations in the SC. The low $\Delta R_{D,0}$ can be related to the degraded Andreev reflection efficiency P_{AR}. From Fig. 1f, we obtained $P_{AR} \sim 0.1$ at $B = 8$ T. Considering the maximum efficiency is bounded by $\Delta R_{D,max}$, we take the product of P_{AR} to $\Delta R_{D,max}$, resulting in $\sim -640\ \Omega$, which is close to $\Delta R_{D,0}$. Since the magnetic field necessary for the QH effect also degrades the CAC, a careful optimization is needed to maximize the CAC process of QH edge states within the constraint.

Discussion for topological superconductivity

Although we mostly focused on the most stable $\nu = 2$ QH state in this study, a negative downstream chemical potential is also clearly observed in the $\nu = 1$ QH state. The spin-polarized (or spinless) $\nu = 1$ QH state is of particular interest as a possible host of Majorana zero modes. It is intriguing to note that the spin-polarized $\nu = 1$ QH state demonstrates the CAC process with a spin singlet s-wave SC, showing a substantially large negative downstream chemical potential. We understand this CAC process to be enabled by the large spin–orbit coupling inherited from the NbN superconducting electrode[37], where spin is no longer a good quantum number. The spin–orbit coupling of superconductors also played an important role for realizing localized Majorana zero modes in a ferromagnetic atomic chain system[38]. The general idea and methodology presented in this work can be readily extended to $\nu = 1$ for hosting Majorana zero modes or to fractional QH states for parafermionic zero modes, opening a new route towards a universal topological quantum computation.

Methods

Methods, including statements of data availability and any associated accession codes and references, are available in the online version of this paper.

Received 28 September 2016; accepted 7 March 2017; published online 3 April 2017

References

1. Rickhaus, P., Weiss, M., Marot, L. & Schönenberger, C. Quantum Hall effect in graphene with superconducting electrodes. *Nano Lett.* **12,** 1942–1945 (2012).
2. Wan, Z. *et al*. Induced superconductivity in high-mobility two-dimensional electron gas in gallium arsenide heterostructures. *Nat. Commun.* **6,** 7426 (2015).
3. Amet, F. *et al*. Supercurrent in the quantum Hall regime. *Science* **352,** 966–969 (2016).
4. Vaezi, A. Fractional topological superconductor with fractionalized Majorana fermions. *Phys. Rev. B* **87,** 035132 (2013).
5. Vaezi, A. Superconducting analogue of the parafermion fractional quantum Hall states. *Phys. Rev. X* **4,** 031009 (2014).
6. Takayanagi, H. & Kawakami, T. Superconducting proximity effect in the native inversion layer on InAs. *Phys. Rev. Lett.* **54,** 2449–2452 (1985).
7. Heersche, H. B., Jarillo-Herrero, P., Oostinga, J. B., Vandersypen, L. M. K. & Morpurgo, A. F. Bipolar supercurrent in graphene. *Nature* **446,** 56–59 (2007).
8. Jeong, D. *et al*. Observation of supercurrent in PbIn-graphene-PbIn Josephson junction. *Phys. Rev. B* **83,** 094503 (2011).
9. Mizuno, N., Nielsen, B. & Du, X. Ballistic-like supercurrent in suspended graphene Josephson weak links. *Nat. Commun.* **4,** 2716 (2013).
10. Lee, G.-H., Kim, S., Jhi, S.-H. & Lee, H.-J. Ultimately short ballistic vertical graphene Josephson junctions. *Nat. Commun.* **6,** 6181 (2015).
11. Calado, V. E. *et al*. Ballistic Josephson junctions in edge-contacted graphene. *Nat. Nanotech.* **10,** 761–764 (2015).
12. Ben Shalom, M. *et al*. Quantum oscillations of the critical current and high-field superconducting proximity in ballistic graphene. *Nat. Phys.* **12,** 318–322 (2015).
13. Efetov, D. K. *et al*. Specular interband Andreev reflections at van der Waals interfaces between graphene and $NbSe_2$. *Nat. Phys.* **12,** 328–332 (2015).
14. Zhang, Y., Tan, Y.-W., Stormer, H. L. & Kim, P. Experimental observation of the quantum Hall effect and Berry's phase in graphene. *Nature* **438,** 201–204 (2005).
15. Bolotin, K. I., Ghahari, F., Shulman, M. D., Stormer, H. L. & Kim, P. Observation of the fractional quantum Hall effect in graphene. *Nature* **462,** 196–199 (2009).
16. Hoppe, H., Zülicke, U. & Schön, G. Andreev reflection in strong magnetic fields. *Phys. Rev. Lett.* **84,** 1804–1807 (2000).
17. Chtchelkatchev, N. M. & Burmistrov, I. S. Conductance oscillations with magnetic field of a two-dimensional electron gas-superconductor junction. *Phys. Rev. B* **75,** 214510 (2007).
18. Khaymovich, I. M., Chtchelkatchev, N. M., Shereshevskii, I. A. & Mel'nikov, A. S. Andreev transport in two-dimensional normal-superconducting systems in strong magnetic fields. *Europhys. Lett.* **91,** 17005 (2010).
19. Clarke, D. J., Alicea, J. & Shtengel, K. Exotic circuit elements from zero-modes in hybrid superconductor-quantum-Hall systems. *Nat. Phys.* **10,** 877–882 (2014).
20. Hou, Z., Xing, Y., Guo, A.-M. & Sun, Q.-F. Crossed Andreev effects in two-dimensional quantum Hall systems. *Phys. Rev. B* **94,** 064516 (2016).
21. Qi, X.-L., Hughes, T. L. & Zhang, S.-C. Chiral topological superconductor from the quantum Hall state. *Phys. Rev. B* **82,** 184516 (2010).
22. Lindner, N. H., Berg, E., Refael, G. & Stern, A. Fractionalizing Majorana fermions: non-Abelian statistics on the edges of Abelian quantum Hall states. *Phys. Rev. X* **2,** 041002 (2012).
23. Clarke, D. J., Alicea, J. & Shtengel, K. Exotic non-Abelian anyons from conventional fractional quantum Hall states. *Nat. Commun.* **4,** 1348 (2013).
24. Mong, R. S. K. *et al*. Universal topological quantum computation from a superconductor-Abelian quantum Hall heterostructure. *Phys. Rev. X* **4,** 011036 (2014).
25. Alicea, J. & Fendley, P. Topological phases with parafermions: theory and blueprints. *Annu. Rev. Condens. Matter Phys.* **7,** 119–139 (2016).
26. Wang, L. *et al*. One-dimensional electrical contact to a two-dimensional material. *Science* **342,** 614–617 (2013).
27. Dynes, R. C., Narayanamurti, V. & Garno, J. P. Direct measurement of quasiparticle-lifetime broadening in a strong-coupled superconductor. *Phys. Rev. Lett.* **41,** 1509–1512 (1978).
28. Naidyuk, Y. G., Häussler, R. & Löhneysen, H. v. Magnetic field dependence of the Andreev reflection structure in the conductivity of S-N point contacts. *Physica B* **218,** 122–125 (1996).
29. Naidyuk, Y. G., Löhneysen, H. v. & Yanson, I. K. Temperature and magnetic-field dependence of the superconducting order parameter in Zn studied by point-contact spectroscopy. *Phys. Rev. B* **54,** 16077–16081 (1996).
30. Eskildsen, M. R. *et al*. Vortex imaging in the π band of magnesium diboride. *Phys. Rev. Lett.* **89,** 187003 (2002).
31. Bugoslavsky, Y. *et al*. Effect of magnetic field on the two superconducting gaps in MgB_2. *Phys. Rev. B* **69,** 132508 (2004).
32. Miyoshi, Y., Bugoslavsky, Y. & Cohen, L. F. Andreev reflection spectroscopy of niobium point contacts in a magnetic field. *Phys. Rev. B* **72,** 012502 (2005).
33. Bandurin, D. A. *et al*. Negative local resistance caused by viscous electron backflow in graphene. *Science* **351,** 1055–1058 (2016).
34. Chockalingam, S. P. *et al*. Tunneling studies in a homogeneously disordered *s*-wave superconductor: NbN. *Phys. Rev. B* **79,** 094509 (2009).
35. Chockalingam, S. P., Chand, M., Jesudasan, J., Tripathi, V. & Raychaudhuri, P. Superconducting properties and Hall effect of epitaxial NbN thin films. *Phys. Rev. B* **77,** 214503 (2008).
36. Mondal, M. *et al*. Enhancement of the finite-frequency superfluid response in the pseudogap regime of strongly disordered superconducting films. *Sci. Rep.* **3,** 1357 (2013).
37. Wakamura, T., Hasegawa, N., Ohnishi, K., Niimi, Y. & Otani, Y. Spin injection into a superconductor with strong spin–orbit coupling. *Phys. Rev. Lett.* **112,** 036602 (2014).
38. Nadj-Perge, S. *et al*. Observation of Majorana fermions in ferromagnetic atomic chains on a superconductor. *Science* **346,** 602–607 (2014).

Acknowledgements

We thank S.-C. Zhang, B. Halperin and J. Alicea for fruitful discussions. The major experimental work, including sample preparation and measurement, is supported by DOE (DE-SC0012260). The Harvard collaboration was supported by the Science and Technology Center for Integrated Quantum Materials, NSF Grant No. DMR-1231319. G.-H.L. acknowledges support from the Nano Material Technology Development Program through the National Research Foundation of Korea (NRF) funded by the Ministry of Science, ICT and Future Planning (2012M3A7B4049966). P.K. acknowledges partial support from the Gordon and Betty Moore Foundation's EPiQS Initiative through Grant GBMF4543 and ARO (W911NF-14-1-0638). K.-F.H. is supported by NSF (EFRI 2-DARE 1542807). A.Y. acknowledges support from the US DOE Office of Basic Energy Sciences, Division of Materials Sciences and Engineering under award de-sc0001819. D.S.W. acknowledges the support from the National Science Foundation Graduate Research Fellowship under Grant No. DGE1144152. K.W. and T.T. acknowledge support from the Elemental Strategy Initiative conducted by the MEXT, Japan and JSPS KAKENHI Grant Numbers JP26248061, JP15K21722 and JP25106006. A portion of this

work was performed at the Center for Nanoscale Systems at Harvard, supported in part by an NSF NNIN award ECS-00335765.

Author contributions

G.-H.L. and P.K. conceived the idea and designed the project. P.K. supervised the project. G.-H.L., K.-F.H. and S.H. fabricated the devices. T.T. and K.W. provided single crystals of hBN. G.-H.L. and D.S.W. performed the measurements. G.-H.L. and P.K. analysed the data and wrote the manuscript. G.-H.L., K.-F.H., D.K.E., D.S.W., S.H., A.Y. and P.K. contributed to the discussion.

Additional information

Supplementary information is available in the online version of the paper. Reprints and permissions information is available online at www.nature.com/reprints. Publisher's note: Springer Nature remains neutral with regard to jurisdictional claims in published maps and institutional affiliations. Correspondence and requests for materials should be addressed to P.K.

Competing financial interests

The authors declare no competing financial interests.

Methods

Fabrication. The superconducting film is optimized for high transparent contact to the graphene channel. After plasma etching of the hBN-encapsulated graphene, 5-nm-thick Ti is electron-beam evaporated at a pressure lower than 1×10^{-8} torr, followed by sputtering 5-nm-thick Nb and 50-nm-thick NbN superconducting films without breaking vacuum. For NbN film, we employ reactive sputtering in an Ar/N_2 environment. A thin layer of Nb film is deposited before the NbN film formation to protect the initial Ti layer from the reactive N radicals during the NbN film growth. The width of the SC is limited by the fabrication process (see Supplementary Fig. 7). The length of the SC electrode ($L \sim 1\,\mu m$) was chosen to ensure the aforementioned asymptotic limit to create the zero-energy resonance mode at the end of the SC electrode. All the other electrodes for source and voltage probes are made of Ti/Au normal metal. We fabricate the contacts by an *in situ* etching scheme[11,12,39] to improve the contact transparency. It is also important to note that there is no graphene left underneath the SC electrode due to the *in situ* etching, leaving a narrow trench of graphene whose edge makes electrical contact to the SC.

Data availability. The data supporting the plots within this paper and other findings of this study are available from the corresponding author on reasonable request.

References

39. Lee, G.-H., Park, G.-H. & Lee, H.-J. Observation of negative refraction of Dirac fermions in graphene. *Nat. Phys.* **11,** 925–929 (2015).